European Journal of Medicinal Chemistry 309 (2026) 118751

Contents lists available at ScienceDirect

European Journal of Medicinal Chemistry

journal homepage: www.elsevier.com/locate/ejmech

Research paper

Photodynamic action of Pd(II)/porphyrin complexes against melanoma cells

Edynara Cruz de Moraes [a,*], Marcos V. Palmeira-Mello [b], Lívia do Carmo Silva [c], Juliana Santana De Curcio [c], Alex Marchezini Graça [b], Jocely Lucena Dutra [b], Antonio Alonso [a], Guilherme Rocha Lino de Souza [d,e], Alzir Azevedo Batista [b,**], Elisângela de Paula Silveira-Lacerda [c], Pablo José Gonçalves [a,f,***]

[a] Institute of Physics, Federal University of Goiás, Goiânia, GO, 74690-900, Brazil
[b] Department of Chemistry, Federal University of São Carlos, São Carlos, SP, 13565-905, Brazil
[c] Laboratory of Oncogenetics and Medical Genetics, Institute of Biological Sciences, Federal University of Goiás, Goiânia, GO, 74690-900, Brazil
[d] Institute of Biological Sciences, Federal University of Goiás, Goiânia, GO, 74690-900, Brazil
[e] Graduate Program in Animal Science, Federal University of Goiás, Goiânia, GO, 74690-900, Brazil
[f] Center of Excellence in Hydrogen and Sustainable Energy Technologies (CEHTES), Goiânia, GO, 74690-900, Brazil

ARTICLE INFO

Keywords:
Photodynamic therapy
Skin cancer
Porphyrin
Singlet oxygen
ROS

ABSTRACT

Photodynamic therapy (PDT) is an emerging strategy for cancer treatment and represents a promising approach for melanoma, one of the most aggressive and therapy-resistant forms of skin cancer. In this study, meso-tetra(4-pyridyl)porphyrin complexes coordinated with palladium(II)/diphosphine ligands (Porf@dppe, Porf@dppp, Porf@dppb, and Porf@dppf; dppe = 1,2-bis(diphenylphosphino)ethane, dppp = 1,3-bis(diphenylphosphino) propane, dppb = 1,4-bis(diphenylphosphino)butane, and dppf = 1,1′-bis(diphenylphosphino)ferrocene), previously shown to display favorable lipophilicity and efficient singlet oxygen production, were evaluated against human (A375) and murine (B16–F10) melanoma cells, as well as non-cancerous keratinocytes (HaCaT). Cytotoxicity measured after a 90 min incubation period yielded dark IC_{50} values between 0.6 and 8.6 μM, whereas light irradiation (λ = 415 nm, 1.8 J cm^{-2}, 36 mW cm^{-2}) resulted in markedly lower IC_{50} values in the nanomolar range (2–27 nM). Irradiation increased intracellular ROS levels, induced morphological alterations in A375 cells, inhibited long-term proliferation, and reduced cell migration, particularly for Porf@dppb and Porf@dppf. The highest cytotoxicity was observed for Porf@dppf, likely due to the redox-active ferrocene unit promoting Fenton-type reactions and enhanced hydroxyl radical formation. Electron paramagnetic resonance (EPR) spin-trapping experiments confirmed light-induced generation of hydroxyl radicals and superoxide anion, with significantly higher hydroxyl radical production observed for Porf@dppf. The photodynamic activity of these complexes is attributed to efficient ROS production involving simultaneous contributions from both Type I and Type II mechanisms. Moderate binding to bovine serum albumin suggests possible albumin-mediated plasma transport. Overall, palladium(II)/diphosphine porphyrin complexes emerge as promising photosensitizers for melanoma photodynamic therapy.

1. Introduction

Melanoma, one of the most aggressive types of skin cancer, presents high metastatic potential and resists conventional therapies. Although melanoma accounts for about 4% of skin cancers, it is highly lethal and causes 75% of skin cancer-related deaths [1]. In recent decades, the incidence of melanoma has increased [2] due to individuals being excessively exposed to ultraviolet radiation originating from sunlight or artificial tanning devices [2], and genetic factors may predispose individuals to develop this type of skin cancer [3]. The global incidence of

* Corresponding author.
** Corresponding author.
*** Corresponding author.
E-mail addresses: edynaramoraes@discente.ufg.br (E. Cruz de Moraes), daab@ufscar.br (A.A. Batista), pablo@ufg.br (P.J. Gonçalves).

https://doi.org/10.1016/j.ejmech.2026.118751
Received 26 November 2025; Received in revised form 20 February 2026; Accepted 4 March 2026
Available online 10 March 2026

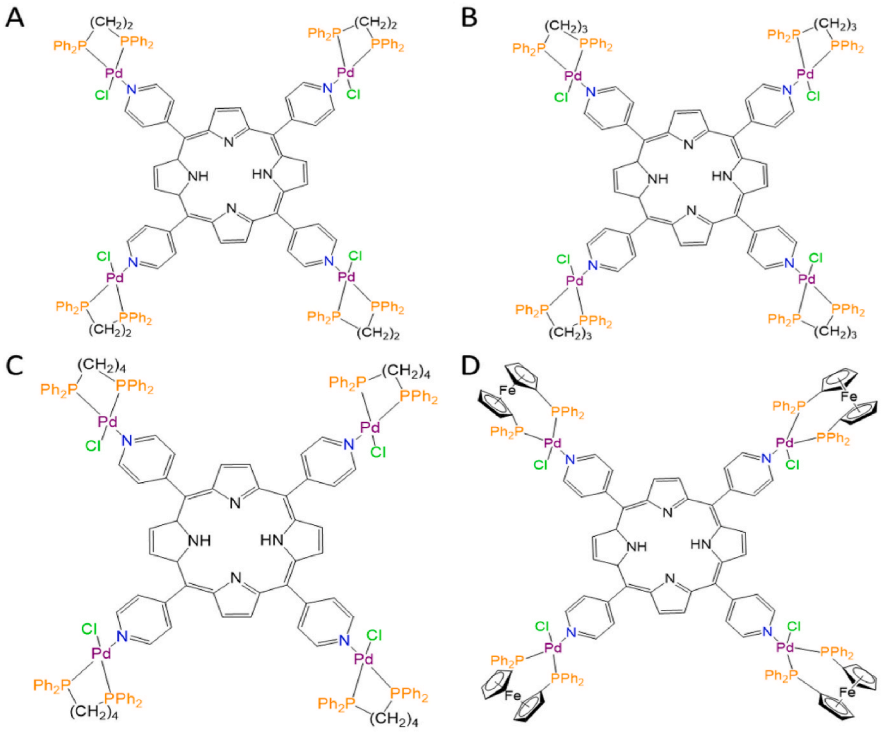

Fig. 1. Representation of the structure of porphyrin complexes: A) Porf@dppe, B) Porf@dppp, C) Porf@dppb, and D) Porf@dppf.

melanoma and its associated mortality are expected to increase substantially by 2040. In 2020, approximately 325,000 new cases of melanoma and 57,000 related deaths occurred worldwide, and about 510, 000 new cases (a 57% increase) and 96,000 related deaths (a 68% increase) are expected in 2040 [4].

Even though advances in targeted therapies, such as BRAF and MEK inhibitors, and immunotherapy have improved some patients' prognoses, these approaches are limited by acquired resistance [5], systemic toxicity [], and high costs [6]. In this context, demand for effective, selective, and affordable therapeutic strategies to treat melanoma has grown, and phototherapy, particularly photodynamic therapy (PDT), has emerged as a promising therapeutic alternative. PDT has proved efficient against not only several microorganisms that are relevant to human and veterinary health [7–9], but also various types of cancer, including melanoma [10–12]. PDT relies on specific light wavelengths to activate photosensitizing agents (PS), to destroy target cells selectively while minimally damaging healthy tissues. Furthermore, several strategies, such as molecular engineering PS, combining PS or therapies, optimizing light delivery systems, and using targeted delivery platforms, have been employed to improve PDT efficiency, to reduce treatment costs, and to enhance therapeutic outcomes [13–19]. Together, these advancements have contributed to making PDT an attractive alternative aiding the expansion of accessibility and improving therapeutic efficacy when treating melanoma.

Metallic porphyrin complexes, particularly complexes containing palladium(II), have been investigated for PDT [20,21]. Palladium shares chemical similarities with platinum, which is known for its anticancer activity in drugs such as cisplatin [22,23] and potentially exerts cytotoxic effects irrespective of irradiation. Moreover, the presence of phosphine ligands in the peripheral positions of the porphyrin complex can enhance its lipophilicity and molecular targeting [24]. This promotes selective cellular uptake of the porphyrin complex and its consequent accumulation in cancer cells, which is critical for therapy [25].

Studies have shown that Pd(II) complexes with pyridyl-substituted porphyrins exhibit promising cytotoxic activity against melanoma cells. Oxidative stress, DNA damage, and induced apoptosis underlie this activity, especially when the complexes are activated by light. Recently, Trentin et al. (2025) [26] investigated two meso-tetra-pyridyl cationic porphyrins (3-PdTPyP and 4-PdTPyP) containing peripheral Pd(II) complexes ($[Pd(bpy)Cl]^+$) and focused on how these porphyrin complexes interact with DNA and induce genotoxic damage and phototoxicity in human (A375) and murine (B16–F10) melanoma cells. Bacterial plasmid assays revealed that the porphyrin complexes preferentially interact with DNA via the minor groove and through van der Waals forces, and that the complexes promote purine oxidation under irradiation with white light, which blocks DNA metabolism. In addition, the porphyrin complexes exhibit selective phototoxicity against melanoma cells: 3-PdTPyP and 4-PdTPyP are more effective against A375 (IC_{50} = 0.43 μM) and B16–F10 (IC_{50} = 0.51 μM) cells, respectively.

Studies have shown that Pd(II) complexes with pyridyl-substituted porphyrins exhibit promising cytotoxic activity against melanoma cells [27,28]. However, previous investigations have primarily focused on general phototoxic responses and overall ROS-mediated damage, without establishing clear correlations between molecular structure and biological performance. In particular, the influence of peripheral diphosphine ligands on cellular behavior, oxidative pathways, and antitumor efficacy remains poorly understood. This lack of structure–activity insight limits rational molecular design and highlights the need for systematic studies addressing how ligand architecture modulates photodynamic responses in melanoma cells.

A series of metalloporphyrin-based photosensitizers (PS), comprising *meso*-tetrapyridyl porphyrins (TPyP) coordinated to palladium(II)–diphosphine complexes, has been designed and synthesized [24]. display notable biological activity, including intrinsic anticancer effects in the absence of light. Photophysical characterization revealed efficient triplet-state formation and singlet oxygen production, supporting their suitability as PS for photodynamic therapy (PDT) [29]. Their therapeutic potential has been further demonstrated by the inactivation of multidrug-resistant bacterial strains isolated from clinical bovine mastitis [30] and by activity against 3D pancreatic tumor models [29]. In light of these results, the present study investigates the phototoxic

effects of these complexes on melanoma cells. To this end, we have evaluated the *in vitro* cytotoxicity of the porphyrin complexes under dark conditions or irradiation with light by using the MTT assay. To gain deeper insight into the biological behavior of these complexes, we have conducted morphological, clonogenic, and migration assays, and we have carried out agarose DNA assays to assess whether these complexes can induce DNA cleavage. We have also investigated how these complexes interact with bovine serum albumin (BSA) to understand how they are transported and biodistributed in biological systems. While previous studies demonstrated the lipophilic nature of these complexes and their efficiency in singlet oxygen generation, electron paramagnetic resonance (EPR) spin-trapping experiments were employed here to further evaluate the formation of hydroxyl radicals and superoxide anion.

1.1. Material and methods

1.1.1. General procedures

All the experimental procedures were performed under an argon atmosphere, to avoid the presence of oxygen and moisture. All chemicals used were of reagent grade or comparable purity. [$PdCl_2(PPh_3)_2$] and the diphosphines (dppe, dppp, dppb and dppf) were used as received from Sigma-Aldrich®. The precursor complexes, *cis*-[$PdCl_2$(P–P)], P–P = dppe, dppp, dppb and dppf, were prepared according to a previously published procedure, without modifications [24].

1.1.2. Synthesis of porphyrin–palladium(II) complexes

The porphyrin complexes investigated herein were synthesized according to previously described procedures [24]. The complexes comprised a series of meso-tetra(4-pyridyl)porphyrins (TPyP) functionalized with peripheral palladium(II) precursors. Each palladium(II) precursor contained a distinct diphosphine ligand: 1,2-*bis*(diphenylphosphino)ethane (dppe), 1,3-*bis*(diphenylphosphino) propane (dppp), 1,4-*bis*(diphenylphosphino)butane (dppb), or 1,1′-*bis*(diphenylphosphino)ferrocene (dppf). For clarity and brevity, the palladium(II) precursors will be designated [$PdCl_2$(dppe)], [$PdCl_2$(dppp)], [$PdCl_2$(dppb)], and [$PdCl_2$(dppf)]; their chemical structures are shown in Fig. S1 and their $^{31}P\{^1H\}$ spectra are in Figs. S2–S5. The corresponding porphyrin-based complexes will be referred to as Porf@dppe, Porf@dppp, Porf@dppb, and Porf@dppf, and their chemical structures are shown in Fig. 1.

Some data used for the characterization of porphyrin complexes are here mentioned:

1.1.3. Porf@dppe

Anal. calc. for $C_{144}H_{122}N_8P_{12}Cl_4F_{24}Pd_4$: calc. (exp.) **C, 51.48** (51.41); **H, 3.66** (3.47); **N, 3.34** (3.12)%. IR (KBr, selected bands, cm^{-1}): 3060 ν(C–H); 1610 ν(CvN); 1429 ν(CvC); 1108 ν(P–C); 848 e 528 ν(P–F); 476 ν(Pd–N). $^{31}P(^1H)$ NMR (162 MHz, DMSO, 298 K): δ (ppm) = 66.61 (s). ^1H NMR (400 MHz, DMSO): δ (ppm) = 9.03 (8H, s, H5 and H5′), 8.86 (8H, s, H2 and H3), 8.28 (8H, s, H4 and H4 ′), 7.73 (30H, m, H of phenyl rings), 7.58 (50H, m, H of phenyl rings), 2.73 (8H, m, CH_2 of ethyl), 2.61 (8H, m, CH_2 of ethyl and H_2O), 2.51 (s, 3H).

1.1.4. Porf@dppp

Anal. calc. for $C_{148}H_{130}N_8P_{12}Cl_4F_{24}Pd_4$: **calc.** (exp.) **C, 52.04** (51.80); **H, 3.83** (3.59); **N, 3.28** (3.00)%. IR (KBr, selected bands, cm^{-1}): 3068 ν(C–H); 1612 ν(C═N); 1423 ν(C═C); 1108 ν(P–C); 858 e 559 ν(P–F); 474 ν(Pd–N). $^{31}P(^1H)$ NMR (162 MHz, DMSO, 298 K): δ (ppm) = 12.79 (broad signal). ^1H NMR (400 MHz, DMSO, 298 K): δ (ppm) = 9.00 (8H, s); 8.81 (8H, s); 8.24 (9H, s); 8.22 (15H, m, H of phenyl rings); 7.82 (s, 15H, m, H of phenyl rings), 7.61 (s, 18H), 7.53 (s, 48H, m, H of phenyl rings); 2.87 (s, 15H,m, CH_2 of propyl), 1.93 (s, 11H, m, CH_2 of propyl).

1.1.5. Porf@dppb

Anal. calc. for $C_{152}H_{138}N_8P_{12}Cl_4F_{24}Pd_4$: **calc**. (exp.) **C, 52.58** (52.20); **H, 4.00** (3.83); **N, 3.28** (3.08)%. IR (KBr, selected bands, cm^{-1})**:** 3066 ν(C–H); 1614 ν(C═N); 1433 ν(C═C); 1093 ν(P–C); 833 e 555 ν(P–F); 486 ν(Pd–N). $^{31}P(^1H)$ NMR (162 MHz, DMSO, 298 K): δ (ppm) = ^1H NMR (400 MHz, DMSO, 298K): δ (ppm) = 9.07 (8H, s, H5 and H5′); 8.05 (8H, s, H2 and H3); 7.74 (8H, s, H4 and H4 ′); 7.69 (26H, m, H of phenyl rings); 7.79–7.56 (51H, m, H of phenyl rings); 3.09 (16H, m, CH_2 of butyl); 1.92 (8H, m, CH_2 of butyl); 1.52 (8H, m, CH_2 of butyl).

1.1.6. Porf@dppf

Anal. calc. for $C_{176}H_{138}N_8Cl_4F_{24}P_{12}Fe_4Pd_4$: **calc.** (exp.) **C, 53.07** (53.15); **H, 3.53** (3.40); **N, 3,00** (2.59)%. IR (KBr, selected bands, cm^{-1}): 3068 ν(C–H); 1612 ν(C═N); 1431 ν(C═C); 1103 ν(P–C); 850 e 553 ν(P–F); 497 ν(Pd–N). $^{31}P(^1H)$ NMR (162 MHz, DMSO, 298 K): δ (ppm) = 37.42 (d,J = 9.4 Hz) and 34.30 (d,J = 8.9 Hz). ^1H NMR (400 MHz, DMSO, 298 K): δ (ppm) = 9.11 (8H, s, H5 and H5′); 8.89 (8H, s, H2 and H3); 8.28 (19H, m, H of phenyl rings); 7.90 (33H, m, H of phenyl rings); 7.62 (17H, m, H of phenyl rings); 7.53 (20H, m, H of phenyl rings); 5.54 (8H, s, CH of ferrocene); 4.89 (8H, s, CH of ferrocene); 4.58 (8H, s, CH of ferrocene); 4.24 (9H, s, CH of ferrocene).

1.2. Biological investigation

1.2.1. Cell culture conditions

Murine melanoma cells (B16–F10), human melanoma cells (A375), and human keratinocytes (HaCaT) were obtained from the Rio de Janeiro Cell Bank (BCRJ, Brazil). All the cells were cultured in Dulbecco's Modified Eagle Medium (DMEM) supplemented with 10% fetal bovine serum (FBS) and maintained in a humidified incubator at 37 °C, with 5% CO_2. DMEM and FBS were obtained from Vitrocell Brasil (Campinas, SP, Brazil) and Gibco Thermo Fisher Scientific (Waltham, MA, USA), respectively.

1.2.2. (Photo)cytotoxicity assay

The cytotoxicity of Porf@dppe, Porf@dppp, Porf@dppb, and Porf@dppf was evaluated by using the 3-(4,5-dimethylthiazol-2-yl)-2,5-diphenyltetrazolium bromide (MTT) assay. A375, B16–F10, or HaCaT cells were used in the experiments. The cells were seeded in 96-well plates at a density of 1×10^4 cells/well and incubated overnight, which allowed 80–90% confluence to be reached.

Stock solutions of Porf@dppe, Porf@dppp, Porf@dppb, and Porf@dppf were prepared in dimethyl sulfoxide (DMSO). Subsequently, the solutions were diluted with DMEM, which provided the desired working concentrations. The final DMSO content in the samples was kept below 0.5%.

To evaluate the cytotoxicity of Porf@dppe, Porf@dppp, Porf@dppb, and Porf@dppf, the cells (A375, B16–F10, or HaCaT cells) were treated with various concentrations of each palladium(II) precursors (0.4 to 50 μM) or one of the porphyrin complexes (0.003 to 12.5 μM). After treatment for 48 h, 50 μL of MTT solution (1 mg/mL) was added to each well, and the cells were incubated for 4 h. The medium was removed, and the formazan crystals were solubilized in 150 μL of DMSO. Absorbance was measured at 540 nm by using a microplate spectrophotometer (Epoch, BioTek). The half-maximal inhibitory concentration (IC_{50}) was calculated with GraphPad Prism 8.0.2. The selectivity index (SI) was determined as the ratio between the IC_{50} obtained for the non-cancerous (HaCaT) and cancer (B16–F10 or A375) cells under equivalent conditions.

For the photocytotoxicity experiments, the cells (A375, B16–F10, or HaCaT cells) were treated with increasing concentrations of Porf@dppe, Porf@dppp, Porf@dppb, or Porf@dppf (0.00019 to 0.00312 μM) and incubated for 90 min, which allowed the cells to internalize the porphyrin complex. After treatment, the culture medium was replaced with fresh medium without phenol red, and the cells were irradiated with a 415-nm LED light source with irradiance of 30 mW/cm^2 for

1 min, which corresponded to a light dose of 1.8 J/cm^2. After incubation for 48 h, 1 mg/mL MTT was added at 37 °C for 3 h. The medium was removed, and the formazan crystals were solubilized in 150 μL of DMSO. Absorbance at 540 nm was measured, and viability was expressed as the percentage relative to the negative control (0.5% DMSO). All the experiments were performed in triplicate and repeated three times. The phototoxicity index (PI) was calculated for each porphyrin complex as the ratio between the IC_{50} determined in the dark and after irradiation with light.

1.2.3. Cell morphology evaluation

The effects of Porf@dppb and Porf@dppf on A375 cell morphology were evaluated using 1×10^4 cells per well seeded in 96-well plates. After 24 h of attachment, the cells were treated with each compound at concentrations corresponding to their previously determined IC_{50} values (7.4 nM for Porf@dppf and 27 nM for Porf@dppb) and at $2 \times IC_{50}$ (14.8 nM for Porf@dppf and 54 nM for Porf@dppb). After incubation for 90 min, which allowed the cells to internalize Porf@dppb or Porf@dppf, the medium was replaced with phenol red-free medium, and the cells were irradiated with a light dose of 1.8 J/cm^2. The cultures were then maintained under standard conditions for 48 h. Morphological changes were assessed at 0 and 48 h by using the CELENA® S Digital Imaging System (Logos Biosystems). For the fluorescence images, after the treatment, the cells were incubated with Hoechst 33258 and propidium iodide for 1 h, and the images were taken by using the CELENA® S Digital Imaging System (Logos Biosystems).

1.2.4. Clonogenic assay

The clonogenic assay was performed to evaluate the long-term proliferative capacity of melanoma cells after PDT. A375 cells were seeded in six-well plates at a density of 500 cells per well. After incubation for 24 h, Porf@dppb or Porf@dppf was added at concentrations corresponding to ½ × IC_{50} (3,7 nM for Porf@dppf and 13,5 nM for Porf@dppb), IC_{50} (7,4 nM for Porf@dppf and 27.0 nM for Porf@dppb), or $2 \times IC_{50}$ (14.8 nM for Porf@dppf and 54 nM for Porf@dppb). The cells were incubated with each PS for 90 min, which allowed the cells to internalize the PS. After that, the medium was replaced with fresh phenol red-free medium. The plates were then irradiated with a light dose of 1.8 J/cm^2 and incubated for seven days, which allowed colonies to form. At the end of this period, the colonies were fixed with methanol/acetic acid (3:1), stained with 0.5% crystal violet in methanol for 30 min, washed with water, and air-dried. All the experiments were performed in triplicate. Relative survival was determined by using the ImageJ software with the "*Colony Area*" plug-in and the "*Analyze Particles*" function, as described in Ref. [31].

1.2.5. Migration assay

To evaluate whether the porphyrin complexes can inhibit cell migration, a wound healing assay was performed. A375 cells were seeded in 24-well plates at a density of 0.5×10^5 cells per well and maintained at 37 °C in humidified 5% CO_2 atmosphere for 24 h. After incubation, a wound was created by using a sterile 200-μL pipette tip. The culture medium was replaced with fresh phenol red-free medium, and the cells were treated with Porf@dppb or Porf@dppf at concentrations corresponding to $^1/_8$ IC_{50} (0,9 nM for Porf@dppf and 3,4 nM for Porf@dppb) or ½ IC_{50} (3,7 nM for Porf@dppf and 13,5 nM for Porf@dppb). After incubation for 90 min, which allowed the cells to internalize Porf@dppb or Porf@dppf, the medium was replaced, and the cells were irradiated with a light dose of 1.8 J/cm^2. The plates were maintained under standard culture conditions, and images of wound closure were captured at 0 and 48 h by using the CELENA® S Digital Imaging System (Logos Biosystems). The wound area was quantified by using the ImageJ software.

1.2.6. Measurement of levels of intracellular reactive oxygen species

Intracellular reactive oxygen species (ROS) production in A375 cells was evaluated by using the fluorescent probe H_2DCFDA. The cells were seeded in DMEM in 24-well plates at a density of 1.0×10^5 cells/well and incubated at 37 °C in humidified atmosphere containing 5% CO_2 for 24 h. Then, the cultures were treated with Porf@dppb or Porf@dppf at concentrations corresponding to ¼ IC_{50} (1,8 nM for Porf@dppf and 6,7 nM for Porf@dppb) or IC_{50} (7.4 nM for Porf@dppf and 27 nM for Porf@dppb) and incubated in the dark for 1 h 30 min. After incubation, the medium was replaced with phenol red-free medium, and the cells were irradiated with a 415-nm LED at a light dose of 1.8 J/cm^2. After irradiation, the medium was removed, and the cells were incubated with H_2DCFDA (10 μM) in the dark at 37 °C for 30 min. The probe was discarded, the cells were washed once with cold PBS, and 200 μL of RIPA lysis buffer was added to each well, which was followed by incubation on ice for 5 min. The cells were detached with a sterile scraper, transferred to microtubes, and centrifuged at 5000 rpm for 5 min. The resulting supernatant was transferred to a black 96-well plate, and DCF fluorescence was measured by using a microplate reader (λ_{exc}: 485 nm, λ_{em}: 535 nm).

1.2.7. Electron paramagnetic resonance (EPR) spectroscopy

Spin trapping EPR experiments were performed under visible light irradiation using a previously described light source (Br. Patent: PI 0802369-7 A2, 2008) equipped with a 500 W halogen lamp, delivering an energy dose of 720 J cm^{-2} [32]. To prevent sample heating, the light beam was passed through a water filter of sufficient thickness to absorb infrared radiation.

EPR measurements were carried out on a Bruker EMX Plus spectrometer (Rheinstetten, Germany) under the following conditions: microwave frequency, 9.83 GHz; microwave power, 20 mW; modulation frequency, 100 kHz; modulation amplitude, 0.5 G; magnetic field scan range, 60 or 80 G; sweep time, 168 s; and sample temperature, 25 °C. Samples consisted of 100 μL aerated porphyrin solutions prepared in DMSO or DMSO:water mixtures. Irradiation was performed for 10 min using the light source described above.

Experimental conditions were applied to detect specific reactive oxygen species: (i) hydroxyl radicals were detected using 80 mM N-*tert*-butyl-α-phenylnitrone (PBN) in DMSO; and (ii) superoxide anion was detected using 25 mM 5,5-dimethyl-1-pyrroline-N-oxide (DMPO) in a 95:5 (v/v) DMSO:water mixture. Control samples lacking porphyrins were prepared in parallel under identical experimental conditions. After irradiation, 30 μL aliquots were transferred to 1 mm inner diameter glass capillaries, flame-sealed, and immediately analyzed by EPR spectroscopy.

1.3. DNA cleavage assay

The potential of Porf@dppb and Porf@dppf to cleave DNA was investigated by agarose gel electrophoresis. The assay was carried out by using pBR322 plasmid DNA in Tris HCl buffer, pH 7.4. The plasmid was incubated with Porf@dppb and Porf@dppf at 12.5 and 25 μM concentrations at 37 °C for 1 h after irradiation with 415 nm light during 10 min (light dose of 1.8 J/cm^2). A gel was prepared by using agarose (1 %) in TAE (Tris-acetate-EDTA) buffer 1x, and the samples were loaded with 10 μL of loading buffer (30% glycerol, 5 mM xylene cyanol). The gel was run in TAE 1x at 50 V and 40 mA for 2 h in a Bio-Rad horizontal tank. The gel was stained with ethidium bromide for 30 min, and the image was obtained by using a Gel Doc EZ Imager instrument (Bio-Rad).

1.4. BSA binding analysis by fluorescence spectroscopy

The BSA (Sigma-Aldrich) interaction with Porf@dppb or Porf@dppf was investigated by accomplishing a fluorescence quenching experiment, where the BSA concentration in buffer (4.5 mM Tris-HCl, 0.5 mM NaOH, and 50 mM NaCl) at pH 7.4 was kept constant (2.5 μM), while the concentration of Porf@dppb or Porf@dppf was increased from 0.031 to 4.0 μM. The emission intensity of the BSA tryptophan residues at 320 nm

Table 1
Main bands (cm^{-1}) in the infrared spectra (KBr pellets).

Complexes	ν(C–H)	ν(C═N)	ν(C═C)	ν(P–C)	ν(P–F)	ν(Pd–N)
Porf@dppe	3060	1610	1429	1108	848 e 528	476
Porf@dppp	3068	1612	1423	1108	858 e 559	474
Porf@dppb	3066	1614	1433	1093	833 e 555	486
Porf@dppf	3068	1612	1431	1103	850 e 553	497

(excitation wavelength of 270 nm) was monitored at 298, 303, and 310 K. The data were analyzed by using the classic Stern−Volmer equation (Eq. (1))

$$\frac{F_0}{F} = 1 + K_{SV}[Q] = 1 + k_q\tau_0[Q] \quad \text{Eq. 1}$$

where F_0 and F correspond to the fluorescence intensities in the absence and presence of the quencher, respectively; [Q] is the concentration of the quencher; and K_{sv} the Stern−Volmer quenching constant. The binding constant (K_b) as well as the number of binding sites (n) was determined by plotting the double log graph of the fluorescence data using Eq (2).

$$log\left[\frac{F_0 - F}{F}\right] = log\, K_b + n\, log[Q] \quad \text{Eq. 2}$$

The thermodynamic parameters ΔH, ΔS, and ΔG were obtained using Eq. (3) and Eq. 4

$$ln\left[\frac{K_2}{K_1}\right] = \left[\frac{1}{T_1} - \frac{1}{T_2}\right]\frac{\Delta H}{R} \quad \text{Eq. 3}$$

$$\Delta G = -RT\, ln\, Kb = \Delta H - T\Delta S \quad \text{Eq. 4}$$

where K_1 and K_2 are the binding constants at temperatures T_1 and T_2, respectively; and R is the gas constant.

1.5. Statistical analysis

The GraphPad Prism software program was used to examine the statistical data collected from the experiment. The data were assessed by using analysis of variance (ANOVA), and any variances in the mean were compared by using the Tukey method. The findings are displayed as the mean with the corresponding standard deviation. A significance level of $P < 0.05$ was used to determine the significance of any observed differences.

2. Results

2.1. General characterization

The palladium metalloporphyrins were obtained by the reactions of the precursors [$PdCl_2$(P–P)] (P–P = dppe, dppp, dppb, dppf) with TpyP porphyrin. In order to complete the formation of the metalloporphyrin species, the $AgPF_6$ salt was employed, in the ratio of 1:1 ($AgPF_6$/Pd precursor), helping the exchange of the chlorido ligand by the nitrogen atoms of TPyP.

In the IR spectra of the metalloporphyrins (Figs. S6, S9, S12 and S15) the main bands of interest are ν(CvN) referring to the porphyrin, ν(P–C) from the phosphines, ν(CvC) from both ligands, ν(P–F) from the counter ion PF_6^- and ν(Pd–N) evidencing the coordination of the Pd precursor to the TPyP periphery, which are displayed in Table 1.

The ^{1}H NMR spectra of the metalloporphyrins were useful for the characterization of the complexes (Figs. S8, S11, S14 and S17). These spectra are can be divided into three parts, the first upfield region corresponding to the hydrogen atoms of the tetrapyrrole macrocycle. The second region, around δ 1.5–3.5 ppm, displays the signals referring to the aliphatic hydrogens of the complexes containing the dppe, dppp and dppb diphosphines. For complex Porf@dppf (Fig. S17) this second region is displaced downfield (δ 3.5–6.0 ppm), mainly due the deshielding effect exerted by the ferrocene iron on the hydrogens of the cyclopentadienyl rings. Finally, in the region between δ 7.0–9.0 ppm we can find the signals corresponding to the aromatic rings of TPyP and diphosphines.

Table 2
$^{31}P\{^1H\}$ chemical shift data for the precursor complexes and for the metalloporphyrins, in CH_2Cl_2/D_2O.

Complexes	δ (ppm)	J (Hz)
[$PdCl_2$(dppe)]	64.74 (s)	-
[$PdCl_2$(dppp)]	11.23 (s)	-
[$PdCl_2$(dppb)]	29.28 (s)	-
[$PdCl_2$(dppf)]	33.69 (s)	-
Porf@dppe	66.61 (s)	-
Porf@dppp	11.99; 9.05	25.4; 27.7
Porf@dppb	40.34; 17.94	23.7; 25.1
Porf@dppf	37.41; 34.26	10.3; 9.3

Table 3
– Partition coefficient (Log P), fluorescence quantum yield (Φ_{FL}), triplet state quantum yield (Φ_T), internal conversion quantum yield (Φ_{IC}) and singlet oxygen quantum yield (Φ_Δ) .

Sample	Log P*	Φ_{FL}*	Φ_T**	Φ_{ic}	Φ_Δ**
Porf@dppe	2.15	0.060	0.82	0.12	0.62
Porf@dppp	2.20	0.054	0.72	0.226	0.64
Porf@dppb	2.56	0.047	0.83	0.123	0.67
Porf@dppf	3.10	0.018	0.46	0.522	0.42

*ref. [24] and ** ref [29].

In the $^{31}P\{^1H\}$ spectra of the precursors in CH_2Cl_2/D_2O (Figs. S2–S5), only singlet signals are observed, since the atoms *trans* to the phosphorus atoms are exclusively chlorine atoms and metalloporphyrins with dppp, dppb, dppf in DMSO (Figures. S10, S13 and S16), presented two doublets, showing the nonequivalence of the phosphorus atoms from the diphosphine, but the compound with the dppe (Fig. S7) ligands showed only a singlet, due to the overlap of the signals. Also, a septet signal at about −144 ppm, belonging to the counterion PF_6^-, was observed in the spectra of the other complexes. All the signs are presented in Table 2.

2.2. Photophysical and physicochemical properties

Comprehensive photophysical characterization is essential to correlate excited-state properties with biological responses, confirm a photodynamic mechanism, and enable comparison with established photosensitizers, thereby supporting the development of safer and more efficient systems. The photophysical and physicochemical properties of the complexes investigated here have been previously reported [24,29] and serve as reliable indicators of their potential for photodynamic applications. Table 3 summarizes the previously determined parameters, including the partition coefficient (Log P) and the quantum yields of fluorescence (Φ_{FL}), triplet state formation (Φ_T), and singlet oxygen production (Φ_Δ) [24,29].

The internal conversion quantum yield (Φ_{IC}) was calculated using Equation (5), considering that S_1 deactivation occurs predominantly through radiative decay via fluorescence (FL), intersystem crossing (ISC), and internal conversion (IC), while other pathways are negligible under the experimental conditions. The obtained results are summarized in Table 3.

$$\Phi_{IC} = 1 - (\Phi_{FL} + \Phi_T) \quad \text{Eq. 5}$$

While Porf@dppe, Porf@dppp, and Porf@dppb display comparable lipophilicity and photophysical properties, Porf@dppf differs by exhibiting higher lipophilicity and reduced singlet oxygen production. This behavior is consistent with its higher Φ_{IC}, indicating that a larger fraction of the excited-state energy is dissipated through non-radiative

Table 4
IC_{50} (μM) of the palladium(II) precursors and their corresponding porphyrin complexes against cancer cell lines (A375 and B16–F10) and a non-cancerous cell line (HaCaT) under dark conditions.

Complex	HaCat	A375	B16–F10	*SI[1]	*SI[2]
[$PdCl_2$(dppf)]	4.2 ± 0.2	3.1 ± 0.3	6.3 ± 0.6	1.3	0.7
[$PdCl_2$(dppp)]	>50	>50	>50	-	-
[$PdCl_2$(dppe)]	>50	>50	>50	-	-
[$PdCl_2$(dppb)]	>50	>50	>50	-	-
Porf@dppf	0.6 ± 0.1	0.9 ± 0.1	1.6 ± 0.1	0.7	0.4
Porf@dppp	2.2 ± 0.3	1.8 ± 0.1	3.2 ± 0.3	1.2	0.7
Porf@dppe	1.7 ± 0.1	4.3 ± 0.6	8.6 ± 0.9	0.4	0.2
Porf@dppb	8.5 ± 0.6	5.1 ± 0.3	8.4 ± 1.1	1.6	1.0

*SI^1=$IC_{50Hacat}/IC_{50A375}$, *SI^2=$IC_{50Hacat}/IC_{50B16-F10}$.

Table 5
IC_{50} (nM) obtained for Porf@dppf, Porf@dppe, Porf@dppp, and Porf@dppb against A375, B16–F10, and HaCaT cells under irradiation with light (LED wavelength of 415 nm, light dose of 1.8 J/cm^2).

Complex	HaCat	A375	B16–F10	PI^1	PI^2	PI^3
Porf@dppf	3.3 ± 0.2	7.4 ± 0.9	1.5 ± 0.4	182	12	1067
Porf@dppe	15.0 ± 3.0	13.0 ± 2.0	25.0 ± 4.0	18	138	128
Porf@dppp	2.1 ± 0.1	5.5 ± 0.7	1.4 ± 0.3	809	860	6143
Porf@dppb	3.2 ± 0.2	27.0 ± 4.0	1.0 ± 0.2	2656	189	8400

The phototoxicity index (PI) was calculated as the ratio $IC_{50dark}/IC_{50light}$ obtained for the same cell line. PI^1 refers to HaCaT cells, PI^2 refers to A375 cells, and PI^3 refers to B16–F10 cells.

relaxation rather than contributing to ISC process and triplet-state formation. Mechanistically, the greater lipophilicity of Porf@dppf may favor intramolecular interactions and increased conformational flexibility in hydrophobic environments, facilitating vibrational and structural relaxation pathways that enhance IC efficiency. As a result, competition with intersystem crossing becomes more pronounced, decreasing the population of the triplet excited state responsible for singlet oxygen generation. This shift in the balance between radiative and non-radiative decay pathways ultimately promotes energy dissipation as heat, leading to lower Φ_Δ values. Overall, these results indicate that these complexes exhibit properties consistent with effective photosensitizers, supporting their potential application in photodynamic therapy.

2.3. *Photo)cytotoxicity studies*

First, the *in vitro* cytotoxicity of palladium(II) porphyrin complexes and their respective precursors was evaluated in cancer (A375 and B16–F10) and non-cancerous (HaCaT) cell lines under dark conditions. The viability curves are presented in the Supplementary Information (Fig. S18–S23), while the corresponding IC_{50} values are summarized in Table 4.

Among the palladium(II) precursors, only [$PdCl_2$(dppf)] exhibited cytotoxicity (IC_{50} = 3.1–6.3 μM), whereas [$PdCl_2$(dppe)], [$PdCl_2$(dppp)], and [$PdCl_2$(dppb)] were inactive at the highest concentration tested (IC_{50} > 50 μM).

Regarding the porphyrin complexes, Porf@dppf exhibited the highest cytotoxicity, with IC_{50} values of 0.9 ± 0.1 and 1.6 ± 0.1 μM against A375 and B16–F10 cells, respectively. However, despite its pronounced activity toward cancer cells, Porf@dppf also showed high cytotoxicity toward HaCaT cells (IC_{50} = 0.6 ± 0.1 μM), resulting in low selectivity (SI < 1). In contrast, Porf@dppb was the least cytotoxic compound, displaying IC_{50} values of 8.5 ± 0.6, 5.1 ± 0.3, and 8.4 ± 1.1 μM against HaCaT, A375, and B16–F10 cells, respectively, but showed higher selectivity indices (SI = 1.6 and 1.0 for A375 and B16–F10 cells, respectively).

Next, we investigated the phototoxicity of the porphyrin complexes under light irradiation. Exposure to light (415 nm, light dose of 1.8 J cm^{-2}) markedly reduced the IC_{50} values of all complexes, which

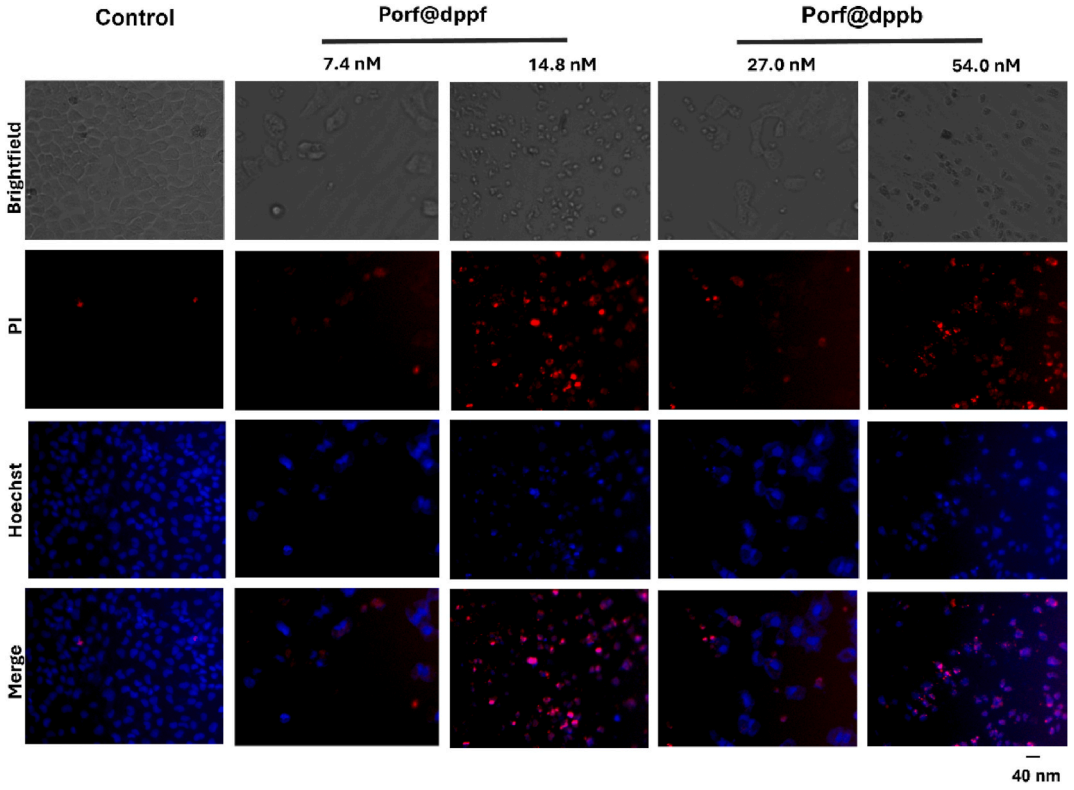

Fig. 2. Morphological analysis of A375 cells treated with Porf@dppb or Porf@dppf and irradiated with light (LED of 415 nm; light dose of 1.8 J/cm^2). Cell nuclei were stained with Hoechst 33528 and propidium iodide (PI).

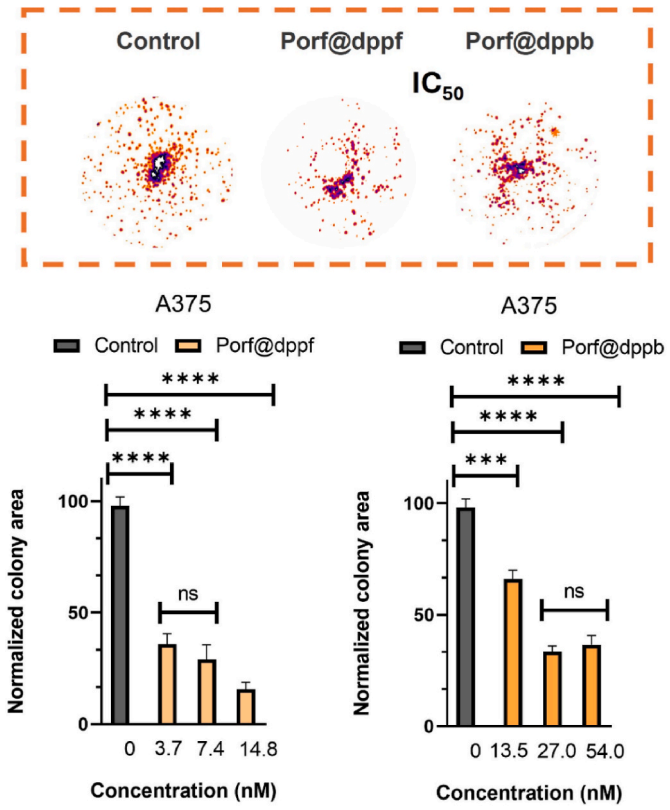

Fig. 3. Clonogenic assay conducted with A375 cells treated with Porf@dppb or Porf@dppf and irradiated with light (LED of 415 nm; light dose of 1.8 J/cm^2). *Above*: Representative images of clonogenic colonies formed in the presence of a porphyrin complex after irradiation with light. *Bellow*: Quantitative analysis of the colony-forming efficiency relative to the control (non-treated) group. Data are presented as the mean ± standard deviation. Different letters indicate statistically significant differences between the groups ($p < 0.05$).

shifted to the nanomolar range (1–27 nM, Table 5). The corresponding cell viability curves are presented in the Supplementary Information (Fig. S24–S26). Among the tested compounds, Porf@dppb exhibited the highest phototoxicity index (PI = 8400) in B16–F10 cells, whereas Porf@dppp showed the highest PI in A375 cells (PI = 860). It is worth noting that the relatively high dark cytotoxicity of Porf@dppf results in lower PI values.

Although the initial cytotoxicity and phototoxicity assays were conducted using three cell lines (A375, B16–F10, and HaCaT), more detailed investigations of cell morphology, clonogenic survival, migration, and ROS generation were performed exclusively in A375 cells treated with Porf@dppb and Porf@dppf, as these complexes displayed the most promising selectivity and cytotoxic profiles.

2.4. Morphological changes

After the cytotoxicity and phototoxicity studies, we evaluated A375 cell morphology in the absence or presence of Porf@dppb or Porf@dppf. In the control group, consisting of untreated A375 cells (in the absence of porphyrin complexes), the cells exhibited typical morphology and formed a confluent monolayer of well-adhered cells with condensed nuclei stained by Hoechst and minimal propidium iodide fluorescence, confirming cell viability and preservation of plasma membrane integrity.

Upon treatment with the compounds at their respective IC_{50} concentrations (7.4 nM for Porf@dppf and 27.0 nM for Porf@dppb), followed by light irradiation, pronounced morphological alterations were observed in A375 cells after 48 h. These changes included reduced confluence, cell rounding, loss of adhesion, and cellular swelling. Hoechst staining revealed nuclear fragmentation, while propidium iodide fluorescence indicated that a fraction of the cell population exhibited compromised membrane integrity.

At 2 × IC_{50} (14.7 nM for Porf@dppf and 54.0 nM for Porf@dppb), these effects became more pronounced, with bright-field images showing an almost complete collapse of the monolayer and the appearance of small apoptotic cell fragments. Nuclear staining revealed a predominance of fragmented nuclei, while increased propidium iodide fluorescence indicated loss of cell viability (Fig. 2).

2.5. Clonogenic response

The antiproliferative effects of Porf@dppb and Porf@dppf on A375 cells were evaluated using clonogenic assays, which assess the ability of a single cell to form colonies comprising at least 50 cells. As shown in Fig. 3, treatment with either complex significantly reduced colony formation, particularly at concentrations corresponding to IC_{50} and 2 × IC_{50} (14.8 nM for Porf@dppf and 54 nM for Porf@dppb). This inhibitory effect was more pronounced for Porf@dppf.

2.6. Inhibition of cell migration

Because cell migration plays a key role in cancer metastasis, the effects of Porf@dppb and Porf@dppf on A375 cell migration were investigated over 24 h using a wound healing assay. The assay was performed in the absence or presence of the complexes under light irradiation. As shown in Fig. 4, both Porf@dppb and Porf@dppf inhibited A375 cell migration following irradiation. This inhibitory effect was more pronounced for Porf@dppf: at ½ IC_{50} (3.7 nM), wound closure reached only ~18% and ~28% in cells treated with Porf@dppf and Porf@dppb, respectively, compared with approximately 76% in the control group (untreated A375 cells).

2.7. Intracellular ROS generation

Intracellular ROS production was evaluated to assess the photodynamic activation potential of the porphyrin complexes. This assay measures oxidative stress generated within cells upon light irradiation, a key mechanism underlying PDT efficacy. In A375 cells treated with the compounds at their respective IC_{50} (7.4 nM for Porf@dppf and 27.0 nM for Porf@dppb), concentrations and subsequently irradiated, intracellular ROS levels increased by approximately 150% compared with the control group. ROS production also showed a concentration-dependent increase, although no significant differences between the complexes were observed (Fig. 5).

2.8. ROS generation: spin trap EPR spectroscopy

Electron paramagnetic resonance (EPR) spin trapping was employed to identify and compare the ROS generated by the porphyrin complexes under visible light irradiation. This analysis is crucial for clarifying the photochemical pathways involved in photodynamic therapy (PDT) and for correlating ROS generation with the biological activity of the photosensitizers.

To compare hydroxyl radical (•OH) generation by the four porphyrins under visible light irradiation, spin trapping experiments were performed using PBN (Fig 6A). Irradiation of PBN in DMSO in the absence of porphyrins led to formation of the PBN–$^{\bullet}$OH adduct, characterized by hyperfine coupling constants of $a_N = 14.0$ G and $a_H = 2.4$ G in DMSO (for comparison, in water a_N = 15.5 G and a_H = 2.7 G), consistent with literature values for hydroxyl radical formation via solvent radiolysis. Under these conditions, all porphyrin complexes generated •OH; however, Porf@dppf exhibited markedly higher hydroxyl radical production than the other complexes.

Superoxide anion ($O_2^{\bullet-}$) formation was evaluated using DMPO,

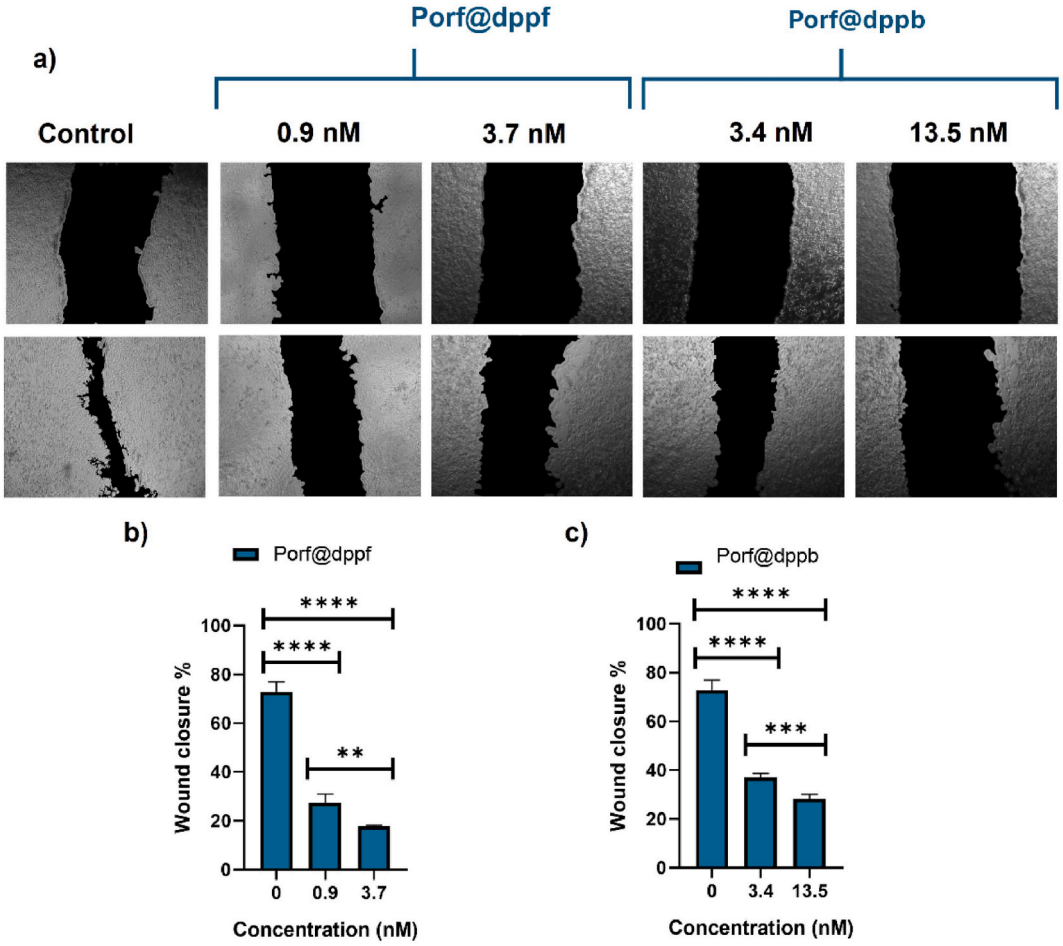

Fig. 4. Migration assay of A375 cells treated with Porf@dppb or Porf@dppf and irradiated with light (LED of 415 nm; light dose of 1.8 J/cm^2). (a) Representative images of the wound healing assay showing cell migration to the scratch area 24 h after treatment, Quantitative analysis of wound closure (%) for cells treated with (b) Porf@dppf and (c) Porf@dppb. Data are presented as the mean ± standard deviation. ns = not significant ($p > 0.05$); **$p < 0.01$; ***$p < 0.001$; ****$p < 0.0001$.

which forms the DMPO–$O_2^{\bullet-}$ adduct characterized by hyperfine coupling constants of $a_N = 13.0$ G, $a_H^{\beta} = 9.8$ G and $a_H^{\gamma} = 1.5$ G [32]. Detection of superoxide requires an aprotic solvent, such as DMSO, typically containing a small fraction of water, since in purely aqueous solutions $O_2^{\bullet-}$ rapidly undergoes dismutation to hydrogen peroxide and molecular oxygen [33]. Aprotic solvents stabilize superoxide by suppressing proton-mediated reactions, as disproportionation to O_2^{2-} is thermodynamically unfavorable under these conditions [34]. In a 95:5 (v/v) DMSO:water mixture, irradiation of the four porphyrins (95 μM) for 10 min resulted in detectable superoxide formation. Porf@dppb and Porf@dppf produced similar and higher signal intensities, whereas Porf@dppe and Porf@dppp generated comparatively lower levels of superoxide (Fig. 6B).

2.9. DNA cleavage properties

In the next part of our study, we used agarose gel electrophoresis to investigate whether Porf@dppb or Porf@dppf promotes DNA cleavage under light irradiation. For this purpose, we employed a pBR322 plasmid DNA. In general, three DNA forms are detected in the gel: supercoiled (SC), open circular (C), and linear (L). These forms present different migration rates, which depend on their size and conformation.

As presented in lanes 1 and 6, the DNA migration rate remained unchanged after light irradiation. Hence, two bands are observed in the gel, corresponding to supercoiled (SC) and open circular (OC) forms (Fig. 7) [35].Porf@dppb seems to cause a single strand break (SSB) producing a linear plasmid, which exhibits a migration between SC and OC forms (lane 2). Furthermore, a higher electrophoretic mobility was observed after increasing the concentration of this compound (lane 3). On the other hand, although Porf@dppf did not alter the DNA mobility at lower concentration (lane 4), it caused a decrease on the mobility of both forms (lane 5) at 25 μM, suggesting alteration in the DNA conformation and/or formation of adducts.

2.10. Serum albumin binding properties

Understanding the interaction between porphyrin complexes and albumin is essential to elucidate their bioavailability and in vivo distribution, thereby enabling optimization of their efficacy as photosensitizers (PS) in photodynamic therapy (PDT). Such interactions can be quantitatively characterized through binding or quenching constants, as well as through thermodynamic and photophysical parameters associated with these processes [36,37].

The interaction between Porf@dppb or Porf@dppf and bovine serum albumin (BSA) was evaluated to assess the potential binding affinity of these photosensitizers for plasma proteins. The addition of Porf@dppb or Porf@dppf led to a concentration-dependent decrease in BSA fluorescence intensity, without causing a shift in the emission maximum (Fig. S27).

Stern–Volmer analysis (Table 6) demonstrated that Porf@dppb and Porf@dppf quenched BSA fluorescence, and that the Stern–Volmer constants (K_{sv}) were in the order of 10^5 (Fig. S28). The biomolecular quenching rate constants ($k_q \sim 10^{13}$ M^{-1} s^{-1}) exceeded the diffusion-controlled limit for biopolymers (7.40×10^9 M^{-1} s^{-1}), which suggests

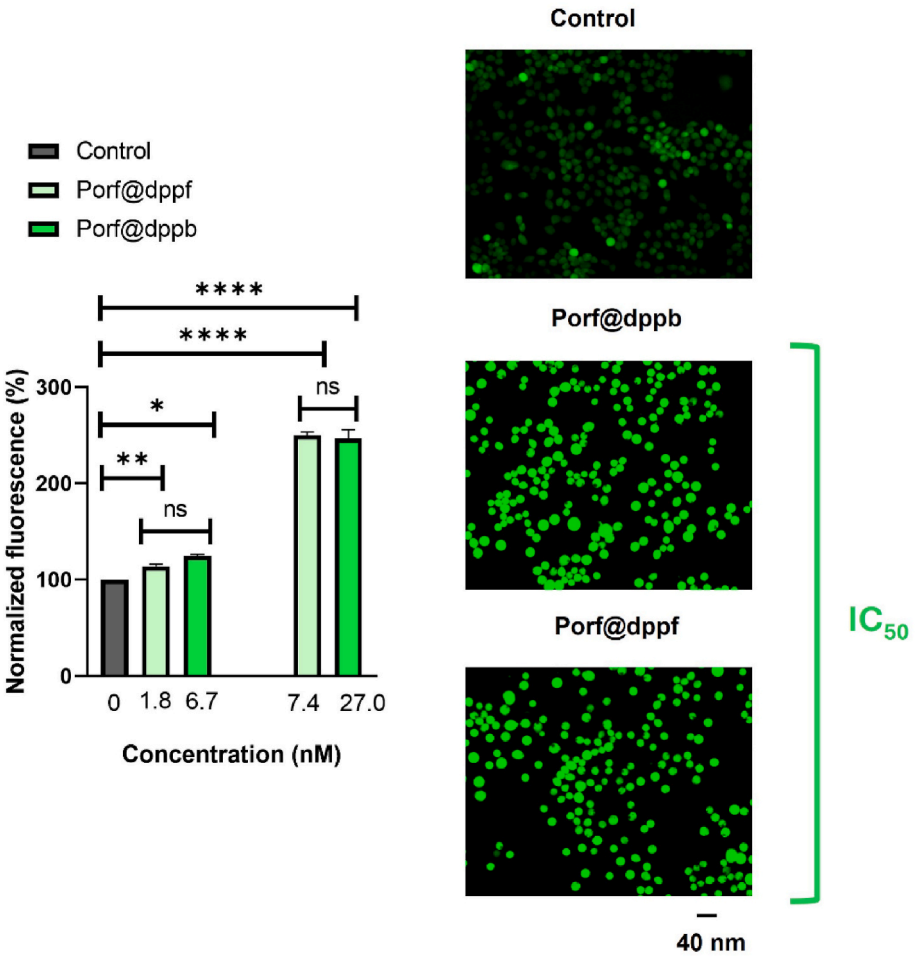

Fig. 5. Intracellular ROS generation in A375 cells treated with Porf@dppb or Porf@dppf under irradiation with light (LED of 415 nm; light dose of 1.8 J/cm^2). Data are presented as the mean ± standard deviation. ns = not significant ($p > 0.05$); *$p < 0.05$; **$p < 0.01$; ****$p < 0.0001$.

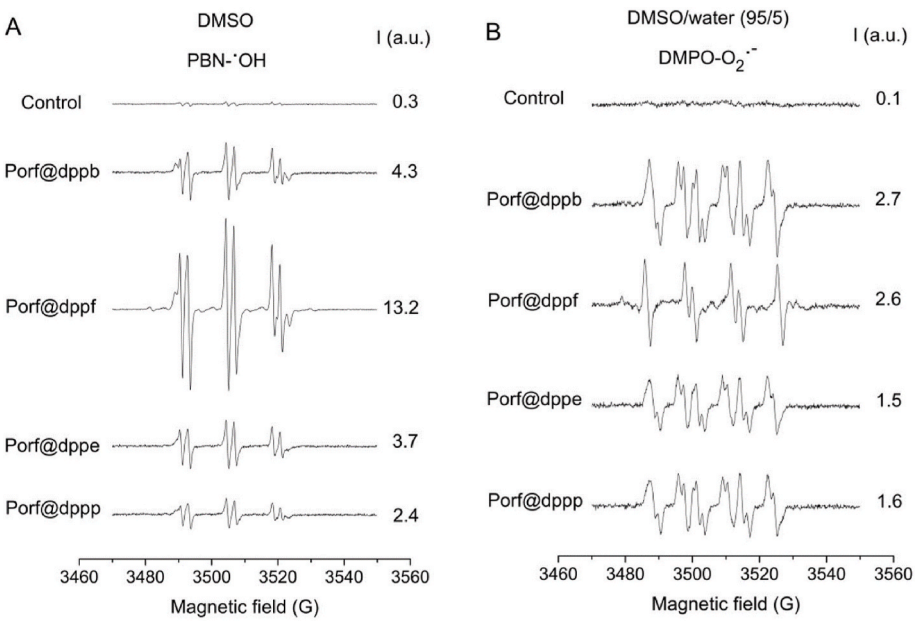

Fig. 6. Representative EPR spectra of the spin traps PBN (panel A), DMPO (panel B) and , recorded in aerated porphyrin solutions after visible light irradiation for 10 min (720 J cm^{-2}). Control samples lacking porphyrins were analyzed in parallel. PBN (80 mM) detected hydroxyl radical adducts (PBN-•OH) for 95 μM porphyrins in DMSO (panel A). DMPO (25 mM) detected superoxide anion adducts (DMPO-$^{\bullet}O^{2-}$) in a 95:5 DMSO:water mixture containing 95 μM porphyrins (panel B). Relative signal intensities are expressed in arbitrary units (y-axis).

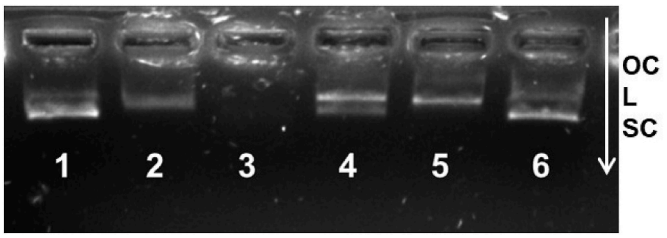

Fig. 7. Agarose gel electrophoresis image of pBR322 plasmid DNA (50 μM) incubated with Porf@dppb and Porf@dppf at 37 °C for 1 h after irradiation during 10 min at 415 nm (light dose of 1.8 J/cm^2). lanes 1 and 6: pure DNA plasmid; lane 2 and 3: DNA treated with Porf@dppb (12.5 and 25 μM); lanes 4 and 5: DNA treated with Porf@dppf (12.5 and 25 μM).

a non-collisional quenching process [38]. Furthermore, K_{sv} did not depend on temperature. The binding constants (K_b) were also in the order of 10^5 L/mol, which indicates that Porf@dppb and Porf@dppf have moderate affinity for albumin [39,40]. We obtained the lowest K_b value for Porf@dppf (1.25×10^5 L/mol) at 298 K, and the number of binding sites (n) was approximately 1, which suggests a 1:1 binding stoichiometry.

The thermodynamic parameters revealed that the Gibbs free energy (ΔG) ranged from −29.1 to −32.0 kJ/mol, which confirms that the interaction is spontaneous. The entropy (ΔS) increased from 85.9 J/mol·K for Porf@dppf to 95.7 J/mol·K for Porf@dppb, while enthalpy (ΔH) became less negative for the latter complex (−3.46 kJ/mol for Porf@dppf and −2.33 kJ/mol for Porf@dppb).

DNA.

3. Discussion

Melanoma remains one of the most challenging targets for photodynamic therapy due to intrinsic resistance mechanisms [40]. A major limitation arises from its high melanin content, which can act as an optical filter by competitively absorbing light and reducing photon penetration, thereby decreasing effective photosensitizer excitation [41]. Among the main components of this pigment, eumelanin and pheomelanin play distinct roles in the photobiological behavior of tumor [42]. Eumelanin exhibits strong antioxidant and photoprotective properties, acting as a scavenger of reactive oxygen species and contributing to the neutralization of PDT-induced oxidative stress [43]. In contrast, pheomelanin has different redox characteristics and, under certain conditions, may participate in the generation of reactive species, potentially enhancing the photodynamic response of melanoma. One strategy to overcome these limitations is the use of optical clearing approaches [44].

In addition to the optical absorption caused by melanin, melanoma also presents well-established hypoxic microenvironments associated with rapid tumor growth and disorganized vascularization. This condition can compromise the efficiency of conventional PDT, since Type II mechanisms depend directly on the availability of molecular oxygen for singlet oxygen generation.

Considering that melanoma is a cutaneous cancer of superficial localization, 415 nm LED light sources have been widely employed in melanoma studies using porphyrins, as this wavelength overlaps with the Soret band and shows proven efficiency in photodynamic activation under blue light [45–47]. Akasov et al. (2019) [48] demonstrated that irradiation with blue light (~450 nm and 5 J/cm^2) in the presence of flavin mononucleotide (FMN) promotes tumor regression (~85–90%) in a murine melanoma model and reduces A375 cell viability (IC_{50} = 10–30 μM), confirming that blue light is effective even in the presence of melanin.

In this context, coordination of meso-tetra(4-pyridyl)porphyrin (TPyP) with peripheral palladium(II)–diphosphine precursors results in enhanced intrinsic cytotoxicity of the corresponding porphyrin complexes under dark conditions. Notably, three of the four precursors—[$PdCl_2$(dppe)], [$PdCl_2$(dppp)], and [$PdCl_2$(dppb)]—displayed low cytotoxicity toward the tested cell lines (IC_{50} > 50 μM). In contrast, [$PdCl_2$(dppf)], which contains a ferrocene moiety, exhibited significantly higher cytotoxicity, with IC_{50} values ranging from 4.2 to 6.3 μM.

Although melanin is often considered one of the main barriers to PDT, upon light irradiation (415 nm), all porphyrin complexes became highly phototoxic, displaying IC_{50} values in the nanomolar range (1–27 nM). Among the tested compounds, Porf@dppb showed the highest phototoxicity index, indicating superior photoinduced cytotoxic efficiency. These results demonstrate that these complexes can overcome melanin-related optical limitations and confirm their strong ROS generation and phototoxic potential. Meanwhile, recently reported and structurally similar porphyrin systems have IC_{50} values in the micromolar range. Martin et al. (2024) [49] reported an IC_{50} of 0.47 ± 0.12 μM against B16–F10 cells under irradiation with 415-nm light (4 J/cm^2). Similarly, Trentin et al. (2024) [26] investigated two palladium(II) porphyrins, 3-PdTPyP and 4-PdTPyP, and showed that they exhibit strong phototoxicity (IC_{50} = 0.43 μM for A375 and 0.51 μM for B16–F10) under LED irradiation (50 mW/cm^2, 90 min, 270 J/cm^2).

From a structural standpoint, Porf@dppe, Porf@dppp, and Porf@dppb are closely related. However, Porf@dppb exhibited superior photodynamic efficacy, which can be attributed to a combination of properties. Among these complexes, Porf@dppb showed higher lipophilicity, more efficient triplet-state formation, enhanced singlet oxygen generation, and increased production of hydroxyl radicals and superoxide. This profile indicates that its activity results from favorable cellular uptake associated with its lipophilic character, together with the concurrent contribution of both Type I and Type II photodynamic pathways.

Although Porf@dppf displayed lower triplet-state and singlet oxygen yields, it presented the highest lipophilicity overall and was the most effective in generating hydroxyl radicals and superoxide. Its photodynamic performance is therefore mainly associated with its strong lipophilic nature and pronounced Type I contribution. In addition, the ferrocene iron center may enhance intracellular redox cycling through Fenton-type reactions, promoting hydrogen peroxide decomposition and hydroxyl radical formation, consistent with the EPR results.

The ability of these complexes—particularly Porf@dppb and Porf@dppf—to operate through both Type I and Type II mechanisms is especially relevant under hypoxic conditions. Their substantial production of hydroxyl radicals and superoxide suggests maintained photodynamic efficiency even in the oxygen-limited tumor microenvironment characteristic of melanoma.

Table 6
Binding constants and thermodynamic data for the interaction between Porf@dppb or Porf@dppf and BSA. Stern–Volmer quenching constant (K_{sv}), bimolecular quenching rate constant (K_q), binding constant (K_b), number of binding sites (n), and thermodynamic parameters (ΔH°, ΔS°, and ΔG°) for the interaction between Porf@dppb or Porf@dppf and BSA at different temperatures (298 and 310 K).

Complex	T (K)	K_{SV} (10^5)	K_q (10^{13})	K_b (10^5)	*n*	ΔH°	ΔS°	ΔG°
Porf@dppb	298	2.32 ± 0.02	3.74	2.57 ± 0.17	0.94	−2.33	95.7	−30.9
	310	2.19 ± 0.10	3.53	2.48 ± 0.30	0.85		95.7	−32.0
Porf@dppf	298	1.17 ± 0.07	1.89	1.25 ± 0.28	0.97	−3.46	85.9	−29.1
	310	1.18 ± 0.03	1.90	1.18 ± 0.41	0.87		85.9	−30.1

Although the selectivity indices of the investigated complexes are not particularly high, which may limit their applicability for systemic administration, this does not diminish their potential relevance for the treatment of superficial melanoma lesions by photodynamic therapy [50,51]. Notably, approximately 70% of newly diagnosed melanoma cases are classified as thin melanomas (TMs), defined by a Breslow thickness of less than 1 mm, which reinforces the clinical relevance of localized therapeutic approaches [52]. In PDT, photosensitizers can be administered directly at the site of interest, and light activation is spatially confined to the irradiated area [53]. As a result, photodynamic damage occurs in a highly controlled and localized manner, leading predominantly to tumor destruction within the illuminated tissue while minimizing adverse effects on surrounding healthy structures [54].

From a pharmacological perspective, the interaction with serum albumin provides important information about the transport and biodistribution of these complexes in biological systems. Since albumin is the main carrier protein in plasma, the observed moderate affinity suggests that the photosensitizers can be efficiently transported in circulation while maintaining stability and availability for tumor uptake. This reversible interaction may favor passive accumulation in tumor tissue while preserving the free fraction required for cellular internalization.

Our results support this interpretation by demonstrating pronounced quenching of BSA fluorescence, indicating the formation of stable ground-state complexes through a static quenching mechanism. The binding constants ($K_b \approx 10^5$ L/mol) reveal moderate and reversible affinity with a 1:1 binding stoichiometry, while thermodynamic parameters (negative ΔG, positive ΔS, and slightly negative ΔH) confirm a spontaneous process predominantly stabilized by electrostatic interactions [8,45–48,55,56]. Together, these findings suggest a favorable profile for plasma transport, stability, and biological availability of the photosensitizers.

Morphological analyses revealed that A375 cells exposed to Porf@dppb or Porf@dppf undergo characteristic apoptotic changes: reduced adhesion, nuclear fragmentation, and collapse of the cell monolayer after 48 h. Wound healing and clonogenic assays further confirmed that, even at low concentrations, Porf@dppb and Porf@dppf inhibit cell migration and colony formation [57].

Furthermore, agarose gel electrophoresis results suggest that Porf@dppb and Porf@dppf act in a dose-dependent manner, altering DNA mobility upon interaction with the double helix [58–60]. The mechanisms through which Porf@dppf or Porf@dppb interact with BSA provide insight into how these porphyrin complexes are transported and biodistributed in biological systems. Given that albumin is the main carrier protein in plasma, its interaction with PS directly influences bioavailability, stability, and tumor-targeting efficiency in PDT [61].

Taken together, these findings indicate that the investigated complexes combine high photodynamic efficiency, strong cellular internalization, and multifactorial ROS generation, maintaining activity even in the presence of melanin and under adverse biological conditions. The achievement of nanomolar IC_{50} values, significantly lower than those reported for structurally related systems, highlights their potential as promising platforms for the development of new photosensitizers for melanoma treatment.

4. Conclusions

Coordinating meso-tetra(4-pyridyl)porphyrin (TPyP) to peripheral palladium(II)–diphosphine complexes modulates the photodynamic properties of TPyP. The presence of the ferrocene moiety increases the intrinsic cytotoxicity of Porf@dppf and enhances oxidative damage and tumor selectivity. Upon visible light irradiation, all investigated porphyrin complexes exhibited pronounced phototoxicity, with IC_{50} values in the nanomolar range, associated with their lipophilic character and DNA fragmentation.

In addition, the porphyrin complexes were shown to produce multiple reactive oxygen species under irradiation, including hydroxyl radicals, superoxide anion, and singlet oxygen. Suggesting simultaneous contribution of both Type I and Type II photodynamic mechanisms. Notably, Porf@dppf displayed substantially higher hydroxyl radical production, consistent with the redox activity of the ferrocene unit and supporting the involvement of Fenton-type processes in its enhanced phototoxic effect. Differences in superoxide and singlet oxygen generation among the complexes further indicate that the diphosphine ligand modulates the balance between ROS pathways, which is likely related to their distinct biological responses.

Moderate and spontaneous interactions between the photosensitizers (PS) and BSA suggest favorable transport in biological media, allowing circulation without permanent sequestration. Overall, these findings provide relevant insights into palladium(II) metalloporphyrins and highlight their potential application in photodynamic therapy (PDT) for melanoma treatment.

CRediT authorship contribution statement

Edynara Cruz de Moraes: Conceptualization, Data curation, Formal analysis, Funding acquisition, Investigation, Methodology, Project administration, Resources, Software, Supervision, Validation, Visualization, Writing – original draft, Writing – review & editing. **Marcos V. Palmeira-Mello:** Data curation, Formal analysis, Funding acquisition, Investigation, Methodology, Resources, Supervision, Validation, Visualization, Writing – original draft, Writing – review & editing. **Lívia do Carmo Silva:** Data curation, Formal analysis, Investigation, Methodology, Supervision, Validation, Writing – original draft, Writing – review & editing. **Juliana Santana De Curcio:** Formal analysis, Investigation, Methodology, Validation, Writing – original draft, Writing – review & editing. **Alex Marchezini Graça:** Investigation, Resources, Visualization. **Jocely Lucena Dutra:** Formal analysis, Investigation, Methodology, Validation, Visualization. **Antonio Alonso:** Conceptualization, Data curation, Formal analysis, Investigation, Methodology, Validation, Visualization, Writing – review & editing. **Guilherme Rocha Lino de Souza:** Conceptualization, Funding acquisition, Resources. **Alzir Azevedo Batista:** Conceptualization, Data curation, Formal analysis, Funding acquisition, Investigation, Methodology, Project administration, Resources, Supervision, Validation, Visualization, Writing – original draft, Writing – review & editing. **Elisângela de Paula Silveira-Lacerda:** Conceptualization, Data curation, Formal analysis, Funding acquisition, Investigation, Methodology, Project administration, Resources, Supervision, Validation, Visualization, Writing – original draft, Writing – review & editing. **Pablo José Gonçalves:** Conceptualization, Data curation, Formal analysis, Funding acquisition, Investigation, Methodology, Project administration, Resources, Software, Supervision, Validation, Writing – original draft, Writing – review & editing.

Declaration of competing interest

The authors declare that they have no known competing financial interests or personal relationships that could have appeared to influence the work reported in this paper.

Acknowledgments

The authors thank the financial support received from the following Brazilian Research Agencies: National Council for Scientific and The National Council for Scientific and Technological Development (CNPq, Grants 406572/2025-9 and 305533/2025-8); National Institute of Science and Technology in Innovative Research in Health Sciences – from Nanotechnology to Artificial Intelligence (INCT PICS) sponsored by Brazil's CNPq (Grants 156117/2021-5, 408417/2024-2 and 305533/2025-8); the São Paulo State Research Foundation (FAPESP, Grants 2023/02475-8 and 2021/01787-0, 2025/26818-7 and 2025/21845-6) and Coordination of Superior Level Staff Improvement (Capes, grant no.

88887.197686/2025-00); and Fundação de Amparo à Pesquisa do Estado de Goiás (FAPEG – 202310267001362).

Appendix A. Supplementary data

Supplementary data to this article can be found online at https://doi.org/10.1016/j.ejmech.2026.118751.

Data availability

No data was used for the research described in the article.

References

[1] L.E. Davis, S.C. Shalin, A.J. Tackett, Current state of melanoma diagnosis and treatment, Cancer Biol. Ther. 20 (2019) 1366–1379, https://doi.org/10.1080/15384047.2019.1640032.
[2] L.-A. Nurla, G. Wafi, R. Tatar, A.M. Dorobanțu, M. Chivu, L.G. Popa, C. Giurcăneanu, O.A. Orzan, Recent-onset Melanoma and the implications of the excessive use of tanning Devices—Case report and review of the literature, Medicina 60 (2024) 187, https://doi.org/10.3390/medicina60010187.
[3] J.E. Hawkes, A. Truong, L.J. Meyer, Genetic predisposition to melanoma, Semin. Oncol. 43 (2016) 591–597, https://doi.org/10.1053/j.seminoncol.2016.08.003.
[4] C. Liu, X. Liu, L. Hu, X. Li, H. Xin, S. Zhu, Global, regional, and national burden of cutaneous malignant melanoma from 1990 to 2021 and prediction to 2045, Front. Oncol. 14 (2024) 1512942, https://doi.org/10.3389/fonc.2024.1512942.
[5] A. Jalil, M.M. Donate, J. Mattei, Exploring resistance to immune checkpoint inhibitors and targeted therapies in melanoma, Cancer Drug Resist (2024), https://doi.org/10.20517/cdr.2024.54.
[6] N. Yousaf, M. Davidson, E. Goode, C. Thomas, R. Hung, M. Gore, J. Larkin, The cost of ipilimumab toxicity: a single-centre analysis, Melanoma Res. 25 (2015) 259–264, https://doi.org/10.1097/CMR.0000000000000158.
[7] A.B. De Freitas, H.H.A. Rezende, G.R.L. De Souza, P.J. Gonçalves, Photodynamic inactivation of KPC-Producing Klebsiella pneumoniae difficult-to-treat resistance (DTR) by a cationic porphyrin, J. Photochem. Photobiol. B Biol. 265 (2025) 113133, https://doi.org/10.1016/j.jphotobiol.2025.113133.
[8] T.M. Dos Anjos Oliveira, A.V. Teles, M.L. Gambarini, K. De Oliveira Ribeiro, E.S. A. Ducas, K.J.G. Dos Santos, C.J.P. Monteiro, E. De Paula Silveira Lacerda, L. P. Franchi, P.J. Gonçalves, G.R.L. De Souza, Photodisinfection of Alphaherpesvirus 1 in bovine semen, J. Photochem. Photobiol. B Biol. 260 (2024) 113036, https://doi.org/10.1016/j.jphotobiol.2024.113036.
[9] L.H.Z. Cocca, T.M.A. Oliveira, F. Gotardo, A.V. Teles, R. Menegatti, J.P. Siqueira, C. R. Mendonça, L.A.M. Bataus, A.O. Ribeiro, T.F.M. Souza, G.R.L. Souza, P. J. Gonçalves, L. De Boni, Tetracarboxy-phthalocyanines: from excited state dynamics to photodynamic inactivation against Bovine herpesvirus type 1, J. Photochem. Photobiol. B Biol. 175 (2017) 1–8, https://doi.org/10.1016/j.jphotobiol.2017.08.019.
[10] V. Papa, F. Furci, P.L. Minciullo, M. Casciaro, A. Allegra, S. Gangemi, Photodynamic therapy in cancer: insights into cellular and molecular pathways, CIMBEBASIA 47 (2025) 69, https://doi.org/10.3390/cimb47020069.
[11] W. Zhao, L. Wang, M. Zhang, Z. Liu, C. Wu, X. Pan, Z. Huang, C. Lu, G. Quan, Photodynamic therapy for cancer: mechanisms, photosensitizers, nanocarriers, and clinical studies, MedComm 5 (2024) e603, https://doi.org/10.1002/mco2.603.
[12] C.S.K. Yeung, S.C.L. Au, Clinical trials update in the photodynamic therapy strategy for treatment of choroidal melanoma: a review of literature, Photodiagnosis Photodyn. Ther. 52 (2025) 104521, https://doi.org/10.1016/j.pdpdt.2025.104521.
[13] R.C. Silva, H.H. Buzzá, E.S.A. Ducas, K.T. Oliveira, V.S. Bagnato, G.R.L. Souza, L. M. Almeida, P.J. Gonçalves, Synergic vascular photodynamic activity by methylene blue-curcumin supramolecular assembly, Spectrochim. Acta Mol. Biomol. Spectrosc. 303 (2023) 123281, https://doi.org/10.1016/j.saa.2023.123281.
[14] Z. Lu, Y. Yao, Y. Zheng, J. Yang, X. Shi, C. Chen, Photodynamic anticancer activity of Arthrospira phycocyanobilin enhanced by metal cobalt ion coordination, Dyes Pigments 245 (2026) 113242, https://doi.org/10.1016/j.dyepig.2025.113242.
[15] X. Wang, D. Luo, J.P. Basilion, Photodynamic therapy: targeting cancer biomarkers for the treatment of cancers, Cancers 13 (2021) 2992, https://doi.org/10.3390/cancers13122992.
[16] L. Zhou, H. Hu, J. Li, Y. Yang, S. Tian, Y. Niu, Y. Liu, X. Zeng, Photodynamic immunotherapy of Ruthenium(II) polypyridyl complexes: application in the treatment of colorectal cancer, J. Inorg. Biochem. 274 (2026) 113056, https://doi.org/10.1016/j.jinorgbio.2025.113056.
[17] F. Zhou, J. Yang, Y. Zhang, M. Liu, M.L. Lang, M. Li, W.R. Chen, Local phototherapy synergizes with immunoadjuvant for treatment of pancreatic cancer through induced immunogenic tumor vaccine, Clin. Cancer Res. 24 (2018) 5335–5346, https://doi.org/10.1158/1078-0432.CCR-18-1126.
[18] W. Cai, T. Sun, C. Qiu, H. Sheng, R. Chen, C. Xie, L. Kou, Q. Yao, Stable triangle: nanomedicine-based synergistic application of phototherapy and immunotherapy for tumor treatment, J. Nanobiotechnol. 22 (2024) 635, https://doi.org/10.1186/s12951-024-02925-3.
[19] A.F. Lopes Martins, T.E. Nogueira, M.O. Morais, S.S. De Sousa-Neto, A.F. Oton-Leite, M.C. Valadares, N.M. Aires Freitas, C.R. Leles, E.F. Mendonça, Cost-effectiveness randomized clinical trial on the effect of photobiomodulation therapy for prevention of radiotherapy-induced severe oral mucositis in a Brazilian cancer hospital setting, Support. Care Cancer 29 (2021) 1245–1256, https://doi.org/10.1007/s00520-020-05607-6.
[20] Z. Wang, Q. Sun, B. Liu, Y. Kuang, A. Gulzar, F. He, S. Gai, P. Yang, J. Lin, Recent advances in porphyrin-based MOFs for cancer therapy and diagnosis therapy, Coord. Chem. Rev. 439 (2021) 213945, https://doi.org/10.1016/j.ccr.2021.213945.
[21] F.P. Dwyer, The role of the metal in porphyrin complexes, in: Haematin Enzymes, Elsevier, 1961, pp. 19–28, https://doi.org/10.1016/B978-1-4831-9646-6.50009-0.
[22] R. Czarnomysy, D. Radomska, O.K. Szewczyk, P. Roszczenko, K. Bielawski, Platinum and palladium complexes as promising sources for antitumor treatments, Indian J. Manag. Sci. 22 (2021) 8271, https://doi.org/10.3390/ijms22158271.
[23] T. Scattolin, V.A. Voloshkin, F. Visentin, S.P. Nolan, A critical review of palladium organometallic anticancer agents, Cell Rep. Phys. Sci. 2 (2021) 100446, https://doi.org/10.1016/j.xcrp.2021.100446.
[24] K.M. Alves, J. Honorato, L.M. Lião, V.S. Velozo-Sa, A.P.M. Guedes, J.D.L. Dutra, A. P. Ayalla, J. Ellena, A.A. Batista, P.J. Gonçalves, *Meso* -Tetra-(4-pyridyl)porphyrin/palladium(ii) complexes as anticancer agents, Dalton Trans. 50 (2021) 16254–16264, https://doi.org/10.1039/D1DT01850G.
[25] K. Nishida, T. Tojo, T. Kondo, M. Yuasa, Evaluation of the correlation between porphyrin accumulation in cancer cells and functional positions for application as a drug carrier, Sci. Rep. 11 (2021) 2046, https://doi.org/10.1038/s41598-021-81725-3.
[26] L.B. Trentin, A.R. Viana, S. Iwersen, B.A. Iglesias, O.A. Chaves, A.P. Schuch, Light exposure of tetra-cationic porphyrins containing peripheral pd(II)-bipyridyl complexes and the induced effects on purified DNA molecule, fibroblast and melanoma cell lines, Photochem. Photobiol. 101 (2025) 565–579, https://doi.org/10.1111/php.14017.
[27] J. Deng, H. Li, M. Yang, F. Wu, Palladium porphyrin complexes for photodynamic cancer therapy: effect of porphyrin units and metal, Photochem. Photobiol. Sci. 19 (2020) 905–912, https://doi.org/10.1039/c9pp00363k.
[28] S. Alarifi, D. Ali, S. Alkahtani, R.S. Almeer, ROS-Mediated apoptosis and genotoxicity induced by palladium nanoparticles in human skin malignant melanoma cells, Oxid. Med. Cell. Longev. 2017 (2017) 8439098, https://doi.org/10.1155/2017/8439098.
[29] E. Cruz De Moraes, L. Do Carmo Silva, J. Santana De Curcio, A.M. Graça, A. A. Batista, E.D.P. Silveira Lacerda, P.J. Gonçalves, Palladium(II)-Complexed *meso* -Tetra(4-pyridyl)porphyrin: photodynamic efficacy in 3D pancreatic cancer models, ACS Omega (2025) 5c09619, https://doi.org/10.1021/acsomega.5c09619 acsomega.
[30] L.H.B. Pires, T.M. Dos Anjos Oliveira, J.C. Desordi, E.S.A. Ducas, L.S. Souza, E. C. De Moraes, A.C. Borsanelli, A.A. Batista, P.J. Gonçalves, G.R.L. De Souza, Breaking antibiotic resistance: Porphyrin-driven photoinactivation and priming effect on mastitis-related MDR bacteria, J. Photochem. Photobiol. B Biol. 271 (2025) 113246, https://doi.org/10.1016/j.jphotobiol.2025.113246.
[31] P.J. Gonçalves, F.C. Bezzerra, A.V. Teles, L.B. Menezes, K.M. Alves, L. Alonso, A. Alonso, M.A. Andrade, I.E. Borissevitch, G.R.L. Souza, B.A. Iglesias, Photoinactivation of Salmonella enterica (Serovar Typhimurium) by tetra-cationic porphyrins containing peripheral [Ru(bpy)2Cl]+ units, J. Photochem. Photobiol. Chem. 391 (2020) 112375, https://doi.org/10.1016/j.jphotochem.2020.112375.
[32] G. Liu, J. Zhao, H. Hidaka, ESR spin-trapping detection of radical intermediates in the TiO2-assisted photo-oxidation of sulforhodamine B under visible irradiation, J. Photochem. Photobiol. Chem. 133 (2000) 83–88, https://doi.org/10.1016/S1010-6030(00)00227-6.
[33] D.T. Sawyer, J.S. Valentine, How super is superoxide? Acc. Chem. Res. 14 (1981) 393–400, https://doi.org/10.1021/ar00072a005.
[34] F.M.S. De Alencar, F.S. Gouveia, G.D.F.S.D. Oliveira, A.L. Andrade, M.A. D. Vasconcelos, A.P. Ayala, A.C.S. Gondim, I.M.M.D. Carvalho, C.A.F. Moraes, M. V. Palmeira-Mello, A.A. Batista, L.G.D.F. Lopes, E.H.S. Sousa, Terpyridine-based ruthenium complexes containing a 4,5-diazafluoren-9-one ligand with light-driven enhancement of biological activity, Dalton Trans. 54 (2025) 1850–1870, https://doi.org/10.1039/D4DT02562H.
[35] P.J. Gonçalves, F.C. Bezerra, L.M. Almeida, L. Alonso, G.R.L. Souza, A. Alonso, S. C. Zílio, I.E. Borissevitch, Effects of bovine serum albumin (BSA) on the excited-state properties of meso-tetrakis(sulfonatophenyl) porphyrin (TPPS4), Eur. Biophys. J. 48 (2019) 721–729, https://doi.org/10.1007/s00249-019-01397-w.
[36] J.N.M. Silva, J.C. Desordi, E.S.A. Ducas, O.A. Chaves, M.E.G. Carmo, A.O. T. Patrocinio, B.A. Iglesias, P.J. Gonçalves, Insights into bovine serum albumin (BSA) photooxidation mediated by mono-cationic porphyrins with Pd(II), Pt(II), and Ru(II) bipyridyl complexes, J. Photochem. Photobiol. Chem. 472 (2026) 116793, https://doi.org/10.1016/j.jphotochem.2025.116793.
[37] P.D. Ross, S. Subramanian, Thermodynamics of protein association reactions: forces contributing to stability, Biochemistry 20 (1981) 3096–3102, https://doi.org/10.1021/bi00514a017.
[38] C. Icsel, V.T. Yilmaz, M. Aygun, B. Cevatemre, P. Alper, E. Ulukaya, Palladium(ii) and platinum(ii) saccharinate complexes with bis(diphenylphosphino)methane/ethane: synthesis, S-phase arrest and ROS-mediated apoptosis in human colon cancer cells, Dalton Trans. 47 (2018) 11397–11410, https://doi.org/10.1039/C8DT02389A.
[39] G.F. Grawe, K.M. Oliveira, C.M. Leite, T.D. De Oliveira, J. Honorato, A.G. Ferreira, E.E. Castellano, M.R. Cominetti, R.S. Correa, A.A. Batista, Ruthenium(ii)-diphosphine complexes containing acylthiourea ligands are effective against lung and breast cancers, Dalton Trans. 51 (2022) 1489–1501, https://doi.org/10.1039/D1DT02851K.
[40] X.-Y. Li, L.-C. Tan, L.-W. Dong, W.-Q. Zhang, X.-X. Shen, X. Lu, H. Zheng, Y.-G. Lu, Susceptibility and resistance mechanisms during photodynamic therapy of

melanoma, Front. Oncol. 10 (2020) 597, https://doi.org/10.3389/fonc.2020.00597.
[41] Y.-Y. Huang, D. Vecchio, P. Avci, R. Yin, M. Garcia-Diaz, M.R. Hamblin, Melanoma resistance to photodynamic therapy: new insights, Biol. Chem. 394 (2013) 239–250, https://doi.org/10.1515/hsz-2012-0228.
[42] S. Ito, K. Wakamatsu, T. Sarna, Photodegradation of eumelanin and Pheomelanin and its pathophysiological implications, Photochem. Photobiol. 94 (2018) 409–420, https://doi.org/10.1111/php.12837.
[43] G. Szewczyk, A. Zadlo, M. Sarna, S. Ito, K. Wakamatsu, T. Sarna, Aerobic photoreactivity of synthetic eumelanins and pheomelanins: generation of singlet oxygen and superoxide anion, Pigment Cell Melanoma Res 29 (2016) 669–678, https://doi.org/10.1111/pcmr.12514.
[44] L.P. Martinelli, I. Iermak, L.T. Moriyama, M.B. Requena, L. Pires, C. Kurachi, Optical clearing agent increases effectiveness of photodynamic therapy in a mouse model of cutaneous melanoma: an analysis by Raman microspectroscopy, Biomed. Opt. Express 11 (2020) 6516, https://doi.org/10.1364/BOE.405039.
[45] S. Nistorescu, A.-M. Udrea, M.A. Badea, I. Lungu, M. Boni, T. Tozar, F. Dumitrache, V.-A. Maraloiu, R.G. Popescu, C. Fleaca, E. Andronescu, A. Dinischiotu, A. Staicu, M. Balas, Low blue dose photodynamic therapy with porphyrin-iron oxide nanoparticles complexes: in vitro study on human melanoma cells, Pharmaceutics 13 (2021) 2130, https://doi.org/10.3390/pharmaceutics13122130.
[46] M. Balas, S. Nistorescu, M.A. Badea, A. Dinischiotu, M. Boni, A. Dinache, A. Smarandache, A.-M. Udrea, P. Prepelita, A. Staicu, Photodynamic activity of TMPyP4/TiO2 complex under blue light in human melanoma cells: potential for cancer-selective therapy, Pharmaceutics 15 (2023) 1194, https://doi.org/10.3390/pharmaceutics15041194.
[47] M.T. Martin, A.B. Becceneri, P.C. Ford, R.S. Da Silva, Chemical approach for obtaining a porphyrin bonded to nitro-ruthenium derivative as a promising photosensitizer for enhancing light irradiation therapy, Inorg. Chem. Commun. 161 (2024) 112138, https://doi.org/10.1016/j.inoche.2024.112138.
[48] R.A. Akasov, N.V. Sholina, D.A. Khochenkov, A.V. Alova, P.V. Gorelkin, A. S. Erofeev, A.N. Generalova, E.V. Khaydukov, Photodynamic therapy of melanoma by blue-light photoactivation of flavin mononucleotide, Sci. Rep. 9 (2019) 9679, https://doi.org/10.1038/s41598-019-46115-w.
[49] M.T. Martin, A.B. Becceneri, P.C. Ford, R.S. Da Silva, Chemical approach for obtaining a porphyrin bonded to nitro-ruthenium derivative as a promising photosensitizer for enhancing light irradiation therapy, Inorg. Chem. Commun. 161 (2024) 112138, https://doi.org/10.1016/j.inoche.2024.112138.
[50] C.A. Robertson, D.H. Evans, H. Abrahamse, Photodynamic therapy (PDT): a short review on cellular mechanisms and cancer research applications for PDT, J. Photochem. Photobiol. B Biol. 96 (2009) 1–8, https://doi.org/10.1016/j.jphotobiol.2009.04.001.
[51] C.A. Morton, R.-M. Szeimies, N. Basset-Seguin, P. Calzavara-Pinton, Y. Gilaberte, M. Hædersdal, G.F.L. Hofbauer, R.E. Hunger, S. Karrer, S. Piaserico, C. Ulrich, A.-M. Wennberg, L.R. Braathen, European dermatology forum guidelines on topical photodynamic therapy 2019 part 1: treatment delivery and established indications – actinic keratoses, Bowen's disease and basal cell carcinomas, Acad Dermatol Venereol 33 (2019) 2225–2238, https://doi.org/10.1111/jdv.16017.
[52] G. Paolino, R. Pampena, S.M. Di Ciaccio, A. Carugno, C. Cantisani, M.R. Di Nicola, L. Losco, G. Bortone, S.R. Mercuri, A. Costanzo, M. Ardigò, M. Valenti, Thin amelanotic and hypomelanotic melanoma: clinicopathological and dermoscopic features, Medicina 60 (2024) 1239, https://doi.org/10.3390/medicina60081239.
[53] Z. Huang, H. Xu, A.D. Meyers, A.I. Musani, L. Wang, R. Tagg, A.B. Barqawi, Y. K. Chen, Photodynamic therapy for treatment of solid tumors — potential and technical challenges, Technol. Cancer Res. Treat. 7 (2008) 309–320, https://doi.org/10.1177/153303460800700405.
[54] M.Z. El-Sadek, M.K.A. El-Aziz, A.H. Shaaban, S.A. Mostafa, A.-H.S. Wadan, Advancements and emerging trends in photodynamic therapy: innovations in cancer treatment and beyond, Photochem. Photobiol. Sci. 24 (2025) 1489–1511, https://doi.org/10.1007/s43630-025-00765-0.
[55] O. Chiarelli-Neto, A.S. Ferreira, W.K. Martins, C. Pavani, D. Severino, F. Faião-Flores, S.S. Maria-Engler, E. Aliprandini, G.R. Martinez, P. Di Mascio, M.H. G. Medeiros, M.S. Baptista, Melanin photosensitization and the effect of visible light on epithelial cells, PLoS One 9 (2014) e113266, https://doi.org/10.1371/journal.pone.0113266.
[56] P. Mroz, J.T. Hashmi, Y.-Y. Huang, N. Lange, M.R. Hamblin, Stimulation of anti-tumor immunity by photodynamic therapy, Expet Rev. Clin. Immunol. 7 (2011) 75–91, https://doi.org/10.1586/eci.10.81.
[57] N.N.P. Da Silva, M.V. Palmeira-Mello, N.O. Acésio, C.A.F. Moraes, J. Honorato, E. E. Castellano, D.C. Tavares, K.M. Oliveira, A.A. Batista, Ru(ii)-diphosphine/N,S-mercapto complexes and their anti-melanoma properties, Dalton Trans. 54 (2025) 605–615, https://doi.org/10.1039/D4DT02575J.
[58] B.S. Vizzotto, R.S. Dias, B.A. Iglesias, L.F. Krause, A.R. Viana, A.P. Schuch, DNA photocleavage and melanoma cells cytotoxicity induced by a meso-tetra-ruthenated porphyrin under visible light irradiation, J. Photochem. Photobiol. B Biol. 209 (2020) 111922, https://doi.org/10.1016/j.jphotobiol.2020.111922.
[59] M.V. Palmeira-Mello, A.B. Caballero, A. Lopez-Espinar, G.P. Guedes, A. Caubet, A. M.T. De Souza, M. Lanznaster, P. Gamez, DNA-interacting properties of two analogous square-planar cis-chlorido complexes: copper versus palladium, J. Biol. Inorg. Chem. 26 (2021) 727–740, https://doi.org/10.1007/s00775-021-01888-2.
[60] X. Jiang, Y. Sun, J. Cen, W. Yang, Y. Liao, L. Shi, D. Lin, H. Liu, A six coordinated Phosphorus(V) corrole bearing two hydroxyl axial ligands: x-ray structure, DNA interaction, photonuclease activity, and cytotoxicity towards tumor cells, ChemistrySelect 6 (2021) 8200–8204, https://doi.org/10.1002/slct.202101974.
[61] A. Di Masi, Human serum albumin: from molecular aspects to biotechnological applications, Indian J. Manag. Sci. 24 (2023) 4081, https://doi.org/10.3390/ijms24044081.